Optical instability and self-pulsing in silicon nitride whispering gallery resonators

Christophe Baker,[1,*] Sebastian Stapfner,[2] David Parrain, [1] Sara Ducci, [1] Giuseppe Leo, [1] Eva M. Weig[2], Ivan Favero[1]

[1]*Université Paris Diderot, Sorbonne Paris Cité, Laboratoire Matériaux et Phénomènes Quantiques, CNRS-UMR 7162, 10 rue Alice Domon et Léonie Duquet, 75013 Paris, France*

[2]*Fakultät für Physik and Center for NanoScience (CeNS), Ludwig-Maximilians-Universität, Geschwister-Scholl-Platz 1, 80539 München, Germany*

**christophe.baker@univ-paris-diderot.fr*

Abstract: We report time domain observations of optical instability in high Q silicon nitride whispering gallery disk resonators. At low laser power the transmitted optical power through the disk looks chaotic. At higher power, the optical output settles into a stable self-pulsing regime with periodicity ranging from hundreds of milliseconds to hundreds of seconds. This phenomenon is explained by the interplay between a fast thermo-optic nonlinearity within the disk and a slow thermo-mechanic nonlinearity of the structure. A model for this interplay is developed which provides good agreement with experimental data and points out routes to control this instability.

OCIS codes: (130.3120) Integrated optics devices; (190.1450) Bistability; (190.3100) Instabilities and chaos; (190.4390) Nonlinear optics, integrated optics; (190.5940) Self-action effects.

References and Links

1. C. Manolatou, M. J. Khan, S. Fan, P. R. Villeneuve, H. A. Haus, and J. D. Joannopoulos, "Coupling of modes analysis of resonant channel add-drop filters," IEEE J. Quantum Electron. **35**(9), 1322–1331 (1999).
2. S. T. Chu, B. E. Little, W. Pan, T. A. Kaneko, S. A. Sato, and Y. A. Kokubun, "An eight-channel add-drop filter using vertically coupled microring resonators over a cross grid," IEEE Photon. Technol. Lett. **11**(6), 691–693 (1999).
3. F. Vollmer, D. Braun, A. Libchaber, M. Khoshsima, I. Teraoka, and S. Arnold, "Protein detection by optical shift of a resonant microcavity," Appl. Phys. Lett. **80**(21), 4057 (2002), doi:10.1063/1.1482797.
4. J. Zhu, S. K. Ozdemir, Y. F. Xiao, L. Li, L. He, D. R. Chen, and L. Yang, "On-chip single nanoparticle detection and sizing by mode splitting in an ultrahigh-Q microresonator," Nat. Photonics **4**(1), 46–49 (2010).
5. Y. Okawachi, K. Saha, J. S. Levy, Y. H. Wen, M. Lipson, and A. L. Gaeta, "Octave-spanning frequency comb generation in a silicon nitride chip," Opt. Lett. **36**(17), 3398–3400 (2011).
6. E. Peter, P. Senellart, D. Martrou, A. Lemaître, J. Hours, J. M. Gérard, and J. Bloch, "Exciton-photon strong-coupling regime for a single quantum dot embedded in a microcavity," Phys. Rev. Lett. **95**(6), 067401 (2005).
7. T. Aoki, B. Dayan, E. Wilcut, W. P. Bowen, A. S. Parkins, T. J. Kippenberg, K. J. Vahala, and H. J. Kimble, "Observation of strong coupling between one atom and a monolithic microresonator," Nature **443**(7112), 671–674 (2006).
8. T. J. Kippenberg, H. Rokhsari, T. Carmon, A. Scherer, and K. J. Vahala, "Analysis of radiation-pressure induced mechanical oscillation of an optical microcavity," Phys. Rev. Lett. **95**(3), 033901 (2005).
9. L. Ding, C. Baker, P. Senellart, A. Lemaitre, S. Ducci, G. Leo, and I. Favero, "High frequency GaAs nano-optomechanical disk resonator," Phys. Rev. Lett. **105**(26), 263903 (2010).
10. L. Ding, C. Baker, P. Senellart, A. Lemaitre, S. Ducci, G. Leo, and I. Favero, "Wavelength-sized GaAs optomechanical resonators with gigahertz frequency," Appl. Phys. Lett. **98**, 113801 (2011).
11. K. H. Lee, T. G. McRae, G. I. Harris, J. Knittel, and W. P. Bowen, "Cooling and control of a cavity optoelectromechanical system," Phys. Rev. Lett. **104**(12), 123604 (2010).
12. A. Andronico, I. Favero, and G. Leo, "Difference frequency generation in GaAs microdisks," Opt. Lett. **33**(18), 2026–2028 (2008).
13. P. S. Kuo, W. Fang, and G. S. Solomon, "4-quasi-phase-matched interactions in GaAs microdisk cavities," Opt. Lett. **34**(22), 3580–3582 (2009).
14. A. E. Fomin, M. L. Gorodetsky, I. S. Grudinin, and V. S. Ilchenko, "Nonstationary nonlinear effects in optical microspheres," J. Opt. Soc. Am. B **22**(2), 459–465 (2005).

15. C. Schmidt, A. Chipouline, T. Pertsch, A. Tünnermann, O. Egorov, F. Lederer, and L. Deych, "Nonlinear thermal effects in optical microspheres at different wavelength sweeping speeds," Opt. Express **16**(9), 6285–6301 (2008), doi:10.1364/OE.16.006285.
16. T. J. Johnson, M. Borselli, and O. Painter, "Self-induced optical modulation of the transmission through a high-Q silicon microdisk resonator," Opt. Express **14**(2), 817–831 (2006).
17. W. H. P. Pernice, M. Li, and H. X. Tang, "Time-domain measurement of optical transport in silicon micro-ring resonators," Opt. Express **18**(17), 18438–18452 (2010), doi:10.1364/OE.18.018438.
18. S. Chen, L. Zhang, Y. Fei, and T. Cao, "Bistability and self-pulsation phenomena in silicon microring resonators based on nonlinear optical effects," Opt. Express **20**(7), 7454–7468 (2012).
19. A. Gondarenko, J. S. Levy, and M. Lipson, "High confinement micron-scale silicon nitride high Q ring resonator," Opt. Express **17**(14), 11366–11370 (2009).
20. M. C. Tien, J. F. Bauters, M. J. R. Heck, D. T. Spencer, D. J. Blumenthal, and J. E. Bowers, "Ultra-high quality factor planar Si3N4 ring resonators on Si substrates," Opt. Express **19**(14), 13551–13556 (2011).
21. S. S. Verbridge, J. M. Parpia, R. B. Reichenbach, L. M. Bellan, and H. G. Craighead, "High quality factor resonance at room temperature with nanostrings under high tensile stress," J. Appl. Phys. **99**(12), 124304 (2006).
22. Q. P. Unterreithmeier, T. Faust, and J. P. Kotthaus, "Damping of nanomechanical resonators," Phys. Rev. Lett. **105**(2), 027205 (2010).
23. D. T. H. Tan, K. Ikeda, P. C. Sun, and Y. Fainman, "Group velocity dispersion and self phase modulation in silicon nitride waveguides," Appl. Phys. Lett. **96**(6), 061101 (2010), doi:10.1063/1.3299008.
24. M. L. Gorodetsky, A. D. Pryamikov, and V. S. Ilchenko, "Rayleigh scattering in high-Q microspheres," J. Opt. Soc. Am. B **17**(6), 1051–1057 (2000).
25. G. S. Wiederhecker, L. Chen, A. Gondarenko, and M. Lipson, "Controlling photonic structures using optical forces," Nature **462**(7273), 633–636 (2009).
26. R. M. Camacho, J. Chan, M. Eichenfield, and O. Painter, "Characterization of radiation pressure and thermal effects in a nanoscale optomechanical cavity," Opt. Express **17**(18), 15726–15735 (2009).
27. V. R. Almeida and M. Lipson, "Optical bistability on a silicon chip," Opt. Lett. **29**(20), 2387–2389 (2004).
28. T. Carmon, L. Yang, and K. Vahala, "Dynamical thermal behavior and thermal self-stability of microcavities," Opt. Express **12**(20), 4742–4750 (2004).
29. J. G. E. Gardeniers, H. A. C. Tilmans, and C. C. G. Visser, "LPCVD silicon-rich silicon nitride films for applications in micromechanics, studied with statistical experimental design," J. Vac. Sci. Technol. A **14**(5), 2879–2892 (1996).
30. COMSOL material library.
31. M. Oxborrow, "How to simulate the whispering gallery modes of dielectric microresonator in FEMLAB/COMSOL," Proc. SPIE **6452**(64520J), 64520J (2007).
32. L. Ding, C. Belacel, S. Ducci, G. Leo, and I. Favero, "Ultralow loss single-mode silica tapers manufactured by a microheater," Appl. Opt. **49**(13), 2441–2445 (2010).
33. L. He, Y.-F. Xiao, C. Dong, J. Zhu, V. Gaddam, and L. Yang, "Compensation of thermal refraction effect in high-Q toroidal microresonator by polydimethylsiloxane coating," Appl. Phys. Lett. **93**(20), 201102 (2008).
34. L. W. Luo, G. S. Wiederhecker, K. Preston, and M. Lipson, "Power insensitive silicon microring resonators," Opt. Lett. **37**(4), 590–592 (2012).
35. Y. Okamura, S. Yoshinaka, and S. Yamamoto, "Measuring mode propagation losses of integrated optical waveguides: a simple method," Appl. Opt. **22**(23), 3892–3894 (1983).
36. R. Regener and W. Sohler, "Loss in low-finesse Ti: LiNbO3 optical waveguide resonators," Appl. Phys. B **36**(3), 143–147 (1985), doi:10.1007/BF00691779.
37. C. H. Henry, R. F. Kazarinov, H. J. Lee, K. J. Orlowsky, and L. E. Katz, "Low loss Si_3N_4-SiO_2 optical waveguides on Si," Appl. Opt. **26**(13), 2621–2624 (1987).
38. A. De Rossi, V. Ortiz, M. Calligaro, L. Lanco, S. Ducci, V. Berger, and I. Sagnes, "Measuring propagation loss in a multimode semiconductor waveguide," J. Appl. Phys. **97**(7), 073105 (2005).

1. Introduction

Whispering gallery mode (WGM) based optical resonators have many applications ranging from add-drop filters [1,2], biomolecule sensing [3,4], frequency comb generation [5], cavity QED [6,7] to optomechanics [8–11]. In all these applications, a high optical quality factor (Q) and a small mode volume are desirable for better performance and integration, as well as enhanced light-matter interaction. These characteristics result in high power densities that may lead to a variety of nonlinear effects. While some of these effects have practical applications in nonlinear optics [12,13], others can lead to deleterious device instabilities. An optical instability of thermal origin was reported in suspended silicon dioxide (SiO_2) microspheres [14, 15], leading to a pseudo oscillatory optical output with typical timescale in the millisecond range. In integrated photonics, silicon (Si) microdisk [16] and microring structures have been shown to exhibit a much faster and more regular oscillatory behavior

[17,18] that was assigned to an interplay between thermal and free carrier dynamics. Another platform of unique potential for integrated photonics is silicon nitride (SiN), whose good optical properties allow to obtain extremely high Q optical resonators [19,20]. The material's potential extends to nanomechanics, where its high tensile stress form provides unique mechanical Q factors [21, 22]. Moreover, SiN has a broader transparency region than silicon and benefits from the absence of two photon absorption (TPA) at telecom wavelengths [23]. In consequence, SiN optical resonators are often believed to be immune against instabilities disrupting their silicon counterparts.

Here we report on an optical instability in high-Q SiN WGM resonators. Under continuous-wave pumping, the resonators transit between chaotic-like and self-pulsing regimes for the optical output. A rich variety of timescales and amplitudes are observed depending on operating conditions. In the self-pulsing regime, unprecedentedly long periods of oscillation up to a minute are measured. The phenomenon is explained by an interaction between a fast thermo-optic and slow thermo-mechanic nonlinearity. A model is developed which reproduces experimental data and gives routes to control these instabilities.

2. Silicon nitride optical resonators

Fabrication

The fabrication starts from a commercial (HSG-IMIT) wafer composed from top to bottom of a 300 nm thick layer of high tensile stress Low Pressure Chemical Vapor Deposition (LPCVD) SiN, a 3 µm thick SiO_2 sacrificial layer and a Si substrate. The waveguides and disks are defined by e-beam lithography using a double layer PMMA positive resist. We draw straight optical waveguides 8 µm wide and 3 mm long, extending up to the sample facets (Fig. 1(a)). The central part of the waveguide is symmetrically narrowed down to a width of 900 nm using two 60 µm long linear tapering profiles (inset of Fig. 1(a)). To tune the evanescent coupling to the disk resonator, the gap distance between disk and waveguide is varied around an average value of 400nm. The 900 nm wide straight segment of the taper is 20 µm long. All disks on the sample have a nominal diameter of 20µm. A cobalt etch mask is used to protect the structure during an ICP-RIE dry etch (SF_6 and Ar chemistry) through the SiN layer. The sample facets are then cleaved. Removal of the cobalt etch mask is done in a piranha solution (3 H_2SO_4:1 H_2O_2). Finally the sample is dipped for 15 minutes in buffered oxide etchant (7 NH_4F:1 HF) which selectively etches ~1.5µm of SiO_2, freeing the tapered part of the waveguide and isolating the disk resonator on a SiO_2 pedestal (Fig. 1(b)). The disks' sidewall roughness is hardly visible in a Scanning Electron Microscope (SEM) image (Fig. 1(c)), the biggest features measuring below 10 nm (not shown here).

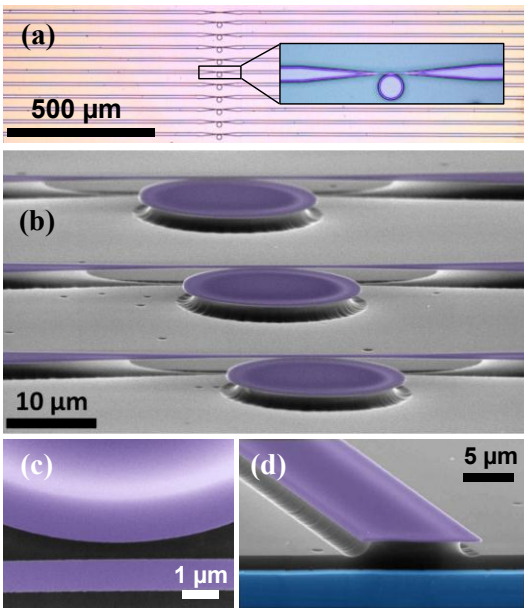

Fig. 1. (a) Optical microscope top view of a sample containing 10 waveguide/disk resonator sets. Inset: tapered part of the waveguide in the disk vicinity. (b) SEM micrograph side view of 3 SiN disk resonators and coupling waveguides. (c) SEM top view of the evanescent coupling region between tapered waveguide and disk. (d) SEM side view of the cleaved waveguide input facet. In (b), (c) and (d) SiN is colored in purple, SiO_2 in gray and Si in blue.

Optical characterization

Optical spectroscopy of each disk couple to its waveguide is performed in the 1500-1600 nm band using a tunable continuous wave external cavity diode laser. The cleaved facets of the waveguide (Fig. 1(d)) serve as optical input/output ports where laser light is injected and collected. The in-plane polarization is selected. Output light is collected by a microscope objective and sent onto a p-i-n photodetector. Figure 2(a) shows the normalized transmission of a guide evanescently coupled to a disk as a function of the laser wavelength. The normalization maintains average unity transmission over the whole wavelength range but keeps fine spectral features. Several resonances appear in this spectrum with a contrast close to unity. They correspond to WGMs with an intrinsic Q factor between 10^5 and $2{\cdot}10^5$. Finer resonances are also present, such as the one shown in Fig. 2(b) which possesses a Q-factor of 4.10^5. In our sample, these resonances tend to have a lower contrast and exhibit doublet splitting due to a symmetry breaking [24]. Because of the positive thermo-optic coefficient ($\partial n/\partial T$) of SiN [25, 26], all optical resonances present a typical bi-stable behavior [27] at high power, which translates into a triangular resonance profile Fig. 2(c) when laser-scanning the resonance.

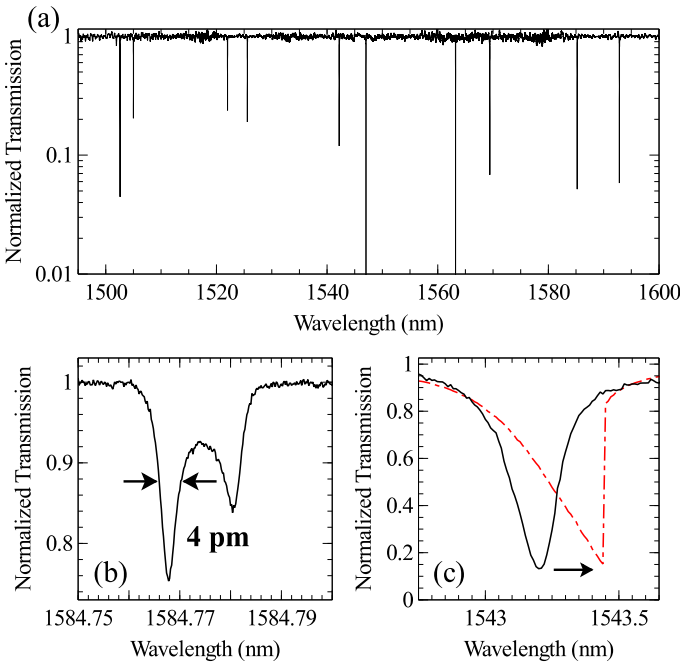

Fig. 2. (a) Optical transmission spectrum of a SiN disk resonator. (b) A fine optical resonance measured in a weakly coupled configuration far from critical coupling, showing an optical Q of 400 000, typical of the highest optical Qs in this device. (c) A broader optical resonance, measured at low power (solid black line) and high power (red dash-dot line).

3. Optical instability

Experimental observation

When the laser wavelength is tuned to the blue detuned flank of a WGM resonance, the positive thermo-optic coefficient of SiN generally provides a negative feedback on the fluctuations in the optical power circulating inside the resonator. Indeed, an increase in the circulating power leads to more heating, which leads to a red-shift of the optical resonance. For a fixed laser wavelength this produces an increased detuning which in turn leads to decreased circulating power. A drop in the optical power is compensated in similar fashion. In this situation the blue detuned flank of a WGM resonance exhibits a thermal self-stability, which is observed routinely on SiO_2 [28] or Gallium Arsenide resonators [10].

The behavior of the present device is in strong contrast with this common case. When the laser wavelength is set slightly blue-detuned to a WGM resonance (red arrow in the inset of Fig. 3(a)), the optical transmission spontaneously settles into a slow periodic oscillatory regime (Fig. 3(a)). The resonator's output alternates between an 'on state' with near unity transmission and the laser out of the WGM resonance, and an 'off state' with near zero transmission and the laser at resonance. While the optical transmission evolves slowly during the on and off states, the switching between the two is extremely sudden (Fig. 3(b)). At high power, the oscillatory behavior maintains a high level of regularity over hundreds of oscillations. The period of the oscillation is found to have an exponential dependence with the optical power circulating in the waveguide, reaching up to nearly 2 minutes for the highest power used in our experiments. The circulating power at the disk level is estimated by taking into account the linear losses in the waveguide from disk to sample facet (see appendix), the reflectivity of the guided mode at the sample facet and the losses in the collection microscope objective. At lower laser power the oscillations in the transmission are still present, however

no longer periodic but resemble a chaotic behavior, with oscillations present at multiple timescales. Characteristic times can be defined for each timescale by an average over a large number of these oscillations. Figure 3(c) shows the transition between the chaotic-like and periodic regimes as the optical power is increased, with measured characteristic times spanning over six orders of magnitude.

These experimental results indicate a complex dynamical behavior, which can be partially uncovered by laser scanning the optical resonances at high power and at different speeds. The red triangular spectrum shown in Fig. 2(c) is acquired with the laser wavelength being swept with a speed of 100 nm/s. Under these conditions and for a WGM resonance width in the 10-100 pm range, the laser wavelength is tuned to the WGM resonance only on the order of 10^{-3}-10^{-4}s. In contrast much slower sweep speeds of the order of 0.01 nm/s, where the resonance is hit during typically one second, result in shifting the resonance center position towards smaller wavelengths (not shown). These distinct behaviors call for the existence of different dynamical phenomena in the system.

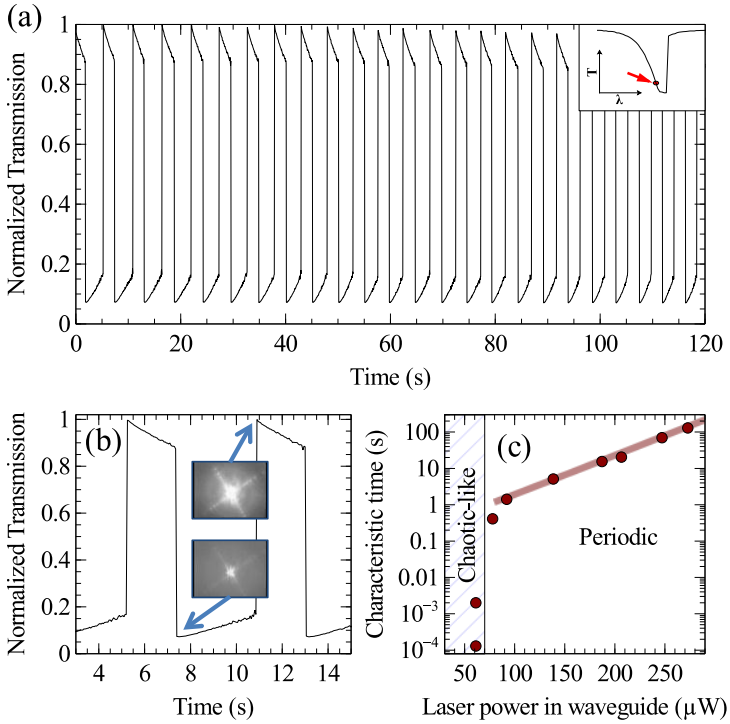

Fig. 3. (a) Normalized optical power measured as a function of time at the output of a waveguide coupled to a SiN disk resonator. The employed WGM resonance at λ = 1539.31 nm has an on-resonance normalized transmission of 7% and a FWHM of 46 pm. It is identified as a p = 1, m = 57 WGM (radial and azimuthal orders). Inset: initial position of laser wavelength λ (red arrow) with respect to the WGM resonance in the transmission T spectrum. (b) Oscillatory behavior shown with greater detail. The inset pictures are single frames from an infrared camera video of the output waveguide transmission taken during measurement (See Media 1). (c) Characteristic time of the oscillatory transmission as a function of the optical power dissipated by the disk. The line through the high power data points is an exponential fit.

Model

Based on the above experimental observation, we develop a model where the fast red-shifting thermo-optic effect competes with a blue shifting effect on a much slower time scale which will be discussed in following. Indeed the thermo-optic effect is associated with the material

temperature within the disk resonator. Given the disk's radius, the thermal conductivity of SiN and the conditions of thermal anchoring to the substrate, the disk's thermal response time is of the order of 7 µs. The much slower phenomenon associated to typical timescales approaching one second remains to be identified. A thermal response time of the substrate may be consistent with such a timescale. In order to test this hypothesis, we develop a simple model. In this model we consider two thermally coupled elements: the disk resonator and a given volume of substrate, both with a uniform temperature field. The disk's temperature T_1 influences the optical resonance position through the thermo-optic effect. In our model we consider that the substrate's temperature T_2 also changes the resonance position, but with an opposite sign effect. Equation (1) expresses the WGM's resonance wavelength λ_{res} as a function of these two parameters in the linear regime:

$$\lambda_{res}(T_1,T_2)=\lambda_{res}(T_0,T_0)+\left(\frac{\partial\lambda_{res}}{\partial T_1}\right)(T_1-T_0)+\left(\frac{\partial\lambda_{res}}{\partial T_2}\right)(T_2-T_0) \qquad (1)$$

where T_0 is the ambient laboratory temperature. The effect on the resonance wavelength of the disk's thermal expansion is an order of magnitude smaller than the thermo-optic contribution. In this limit $(\partial\lambda_{res}/\partial T_1) = (\partial n/\partial T_1)\cdot \lambda_{res}/n$ is a function of the thermo-optic coefficient $(\partial n/\partial T)$ and the refractive index n. In our study $(\partial\lambda_{res}/\partial T_2)$ is a parameter that can be inferred experimentally or computed numerically (see next section). To relate Eq. (1) to an optically measured quantity, we express in Eq. (2) the normalized optical transmission of the resonator Λ as a function of the laser wavelength λ and of temperatures T_1 and T_2. C is the contrast of the WGM resonance (C = 1 for critical coupling and <1 otherwise) and $\delta\lambda$ its full width at half maximum.

$$\Lambda(\lambda,T_1,T_2)=1-\frac{C}{1+\left(\frac{\lambda-\lambda_{res}(T_1,T_2)}{\delta\lambda/2}\right)^2} \qquad (2)$$

This equation relates the resonator's optical transmission to the temperature evolutions. Conversely, the temperature evolutions are governed by the amount of absorbed optical power within the disk, by the thermal contact between the disk and substrate, and by the thermal coupling of the substrate to its environment. We have checked that the thermal coupling of the disk to the surrounding air can be safely neglected. These aspects are cast into the two coupled differential equations Eq. (3) and Eq. (4). Equation (3) gives the rate of change in the disk temperature:

$$\frac{dT_1}{dt}=P_{guide}\,A\,\frac{1-\Lambda(\lambda,T_1,T_2)}{m_1 c_1}-\frac{G_{1,2}}{m_1 c_1}(T_1-T_2) \qquad (3)$$

where P_{guide} is the optical power in the waveguide at the disk level and A is the fraction of the laser power dissipated by the resonator which is absorbed and turned into heat within the disk. The evaluation of this fraction will be discussed below. m_1 is the mass of the SiN disk, c_1 the SiN heat capacity at constant pressure in J K^{-1} kg^{-1} and $G_{1,2}$ the thermal conductance between the disk and substrate in W K^{-1}. $G_{1,2}$ is calculated analytically by summing the thermal resistance between the pedestal and the disk's periphery where light is absorbed with the resistance of the SiO_2 pedestal. In our resonator's geometry we obtain $G_{1,2} = 2.86\cdot10^{-5}$ W K^{-1}, in good agreement with Finite Elements Method (FEM) simulations. Equation (3) contains two terms: the first term is proportional to the optical power lost into the disk and describes the heat inflow, while the second term describes the heat outflow into the substrate.

In a similar manner, the temperature evolution of the substrate volume is written as:

$$\frac{dT_2}{dt} = \frac{G_{1,2}(T_1 - T_2)}{m_2 c_2} - \frac{G_2}{m_2 c_2}(T_2 - T_0) \quad (4)$$

where c_2 is the Si heat capacity at constant pressure, m_2 the mass of the considered volume of substrate and G_2 its thermal conductance to the environment at T_0. The first term of the equation describes the heat inflow from the disk into the substrate, and the second term the heat outflow into the environment. Although the power flow out of the disk $G_{1,2}(T_1\text{-}T_2)$ and incoming power flow into the substrate $G_{1,2}(T_1\text{-}T_2)$ are equal, the dynamical effect on disk and bulk temperature is divided by the mass times the heat capacity of the considered element. Therefore the temperature oscillations in the bulk are significantly smaller than those of the disk.

Comparison between model and experiments

One important ingredient for the above model to explain our experimental results is the correct evaluation of the absorbed optical power Pguide.A (1-Λ). The fraction of laser power absorbed and lost as heat within the disk resonator is calculated by fitting the magnitude of the thermo-optic shift (Fig. 2(c)) on a known resonance, for a typical value of the thermo-optic coefficient ($\partial n/\partial T$) taken from the literature (see table). We find that fraction to be 80 ± 5%. Although this value is high, it is in line with optical losses measured in similarly processed straight SiN waveguides (see appendix). Surface scattering has a minor contribution to total optical losses thanks to the minimal surface roughness obtained with our fabrication process.

Other parameters entering the model are the contrast C and the resonance width δλ, which are directly measured at low optical power on the WGM resonance under consideration, and are independent on the temperature. The value of $(\partial\lambda_{res}/\partial T_1)$ is known from the refractive index and thermo-optic coefficient of SiN. A value of $(\partial\lambda_{res}/\partial T_2)$ is extracted by comparing the WGM optical shift measured at fast and slow laser-scan speeds. For the slow scan-speed, the optical resonance is blue-shifted with respect to the fast scan-speed case. The absorbed optical power is evaluated at low scan-speed and associated to a temperature increase of the substrate by means of FEM thermal simulations. This temperature rise is related to the measured blue-shift, leading to a rough estimate of $(\partial\lambda_{res}/\partial T_2) = \sim 0.27$ nm K^{-1}. This estimate serves as starting value for the fitting procedure where $(\partial\lambda_{res}/\partial T_2)$ is then taken as an adjustable parameter. A second fit parameter is the considered volume of Si substrate. We consider a Si cylinder of equal height and radius h, positioned directly under the pedestal. The cylinder's thermal conductance G_2 is calculated as a function of h using referenced Si thermal conductivities. A summary of physical parameters employed in the model is given in Table 1.

The evolution of the optical transmission coupled dynamically to temperatures T_1 and T_2 through Eqs. (1)–(4) is obtained numerically over 10 million 1μs time steps, yielding results such as the ones shown in Fig. 4. In this figure, we compare the obtained theoretical results to experimental data. In order to recover the richness of the observed oscillatory behavior, we have selected three distinct experimental configurations, with different laser detuning and laser power. In our fitting procedure, the parameters $(\partial\lambda_{res}/\partial T_2)$ and h are varied until we can fit all three sets of measurements with our model using a single set of parameters. The best fit, shown in Fig. 4, is obtained for $(\partial\lambda_{res}/\partial T_2) = 0.227$ nm K^{-1} and h = 500 μm, a height which turns out to match the Si substrate thickness. With these parameters, the disk's thermal response time $\tau_1 = (m_1 \cdot c_1)/G_{1,2}$ is 7.15 μs and the substrate volume's thermal time $\tau_2 = (m_2 \cdot c_2)/G_2$ is 0.58 s. These parameters allow obtaining a very satisfactory agreement between our experimental data and the model, with oscillatory periodic times that span from 0.4 s to 1.4 s in Fig. 4. We also checked that the correct dynamics is reproduced by the model for periodic times going from the millisecond to a few seconds. Figure 5 (a) sketches how the simple model used here reproduces the oscillatory behavior of the optical output.

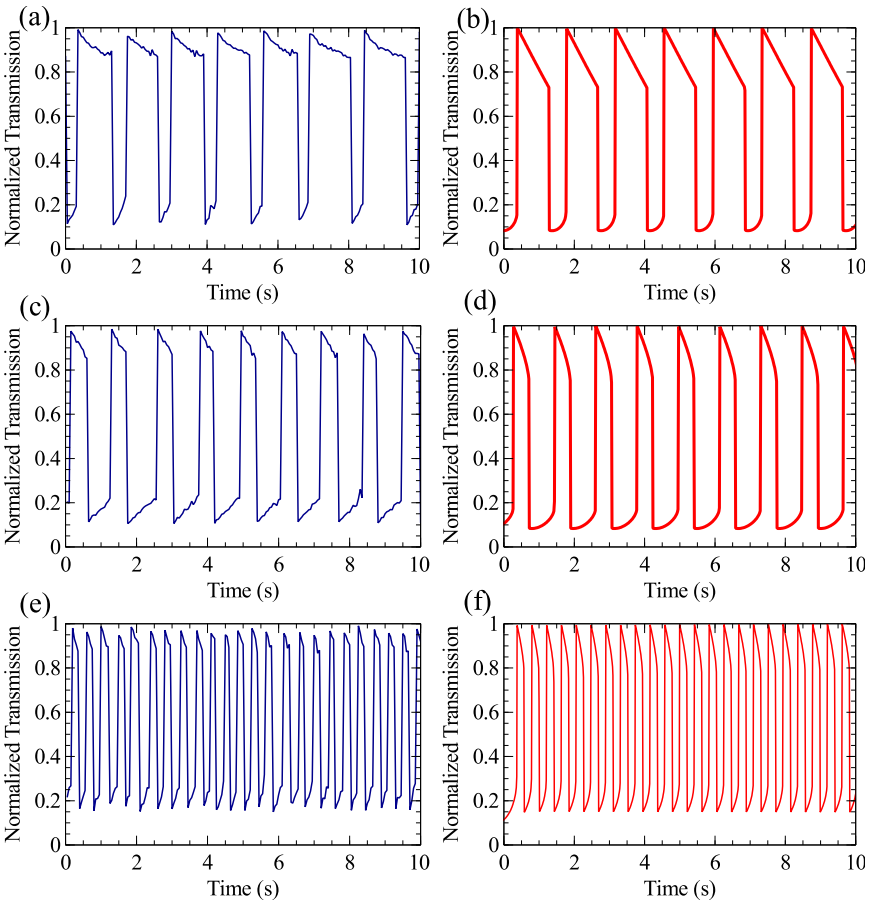

Fig. 4. Experimental (left) and model (right) results for the normalized optical transmission of a WGM resonator for three distinct pump laser configurations. (a) Experiments and (b) model for an initial blue detuned pump configuration with λ = 1539.35 nm and $A \cdot P_{guide}$ = 77 µW. (c) Experiments and (d) model for the same optical power but with initial laser blue detuning 2 pm greater. (e) Experiments and (f) model for a lower power ($A \cdot P_{guide}$ = 65 µW) and for a detuning similar to (a) and (b). In (b), (d) and (f) the temperature oscillations are on the order of a few Kelvin for T_1 and a few tens of mK for T_2.

Table 1. Physical parameters used in the models

Parameter	Name	Unit	Value	Source
SiN refractive index	n	-	2	[29]
SiN thermo-optic coefficient	$(\partial n/\partial T)$	K^{-1}	$2.44 \cdot 10^{-5}$	[25,26]
SiO_2 & Si thermal expansion coefficient		µm m^{-1} K^{-1}	0.5 & 2.6	[30]
SiN & Si heat capacity	c_1 & c_2	J K^{-1} kg^{-1}	700 & 700	[30]
SiN, SiO_2 & Si thermal conductivity		W $m^{-1}K^{-1}$	20, 1.4 & 130	[30]
SiN & Si density		kg m^{-3}	3100 & 2329	[30]
Slow blue-shift coefficient	$(\partial\lambda_{res}/\partial T_2)$	nm K^{-1}	0.227	

4. Origin of the slow thermal nonlinearity

SiO_2 and Si have different thermal expansion coefficients (see Table 1). When these materials are heated by the absorbed laser power within the resonator, this difference leads to stress and structural deformation. Figure 5 (b) shows a simplified 2D axi-symmetric FEM simulation of a SiN disk resonator atop a SiO_2 pedestal on a slab of Si substrate. A uniform increase of the temperature of the Si substrate results in an upward buckling of the whole structure. While the Si substrate expands outward, the SiN disk is bent upwards and slightly inwards, resulting in a reduction in the effective optical WGM cavity radius. This reduction translates into a blue-shift of the WGM resonance, in agreement with the experimental observations at slow time scale. In order to quantify this effect, we use a FEM simulation of the structure including a large-scale substrate slab and accounting for the stress in the SiN layer. For two distinct but close Si substrate temperatures (1K apart), we obtain the disk deformation profile and export it into to a weak-form FEM simulation of the WGM employed in the experiments [31]. This allows for calculating the WGM resonance wavelength shift associated to this differential temperature change and gives a value of $(\partial\lambda_{res}/\partial T_2)$ that agrees within a factor 5 with the value extracted from the model fit. Although these results are in the right order of magnitude, we ascribe the discrepancy to several approximations: first the exact pedestal geometry plays an important role but is not perfectly known, second the temperature profiles of the different elements were taken as uniform, when temperature gradients should influence the exact strain in the real structure. Despite these approximations, our simulations clearly point towards this thermo-mechanic deformation of the structure as being the source of the slow blue-shifting optical nonlinearity.

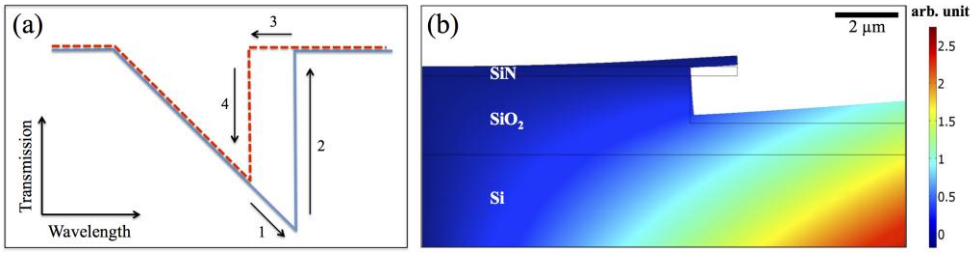

Fig. 5. (a) Schematic description of the regime of self-pulsating optical transmission. In step **1** the laser line starts on the blue-detuned flank of the WGM thermo-optically distorted resonance. The sample substrate slowly heats up, gradually blue-shifting the resonance. Once the resonance wavelength moves past the fixed laser wavelength, the laser line reaches the unstable flank of the thermo-optically distorted resonance: at this stage the WGM snaps out of laser resonance and the transmission jumps back to unity (step **2**). The WGM is out of resonance with the laser and the substrate slowly cools down, gradually red-shifting the optical resonance (step **3**). Finally when the red-shift is sufficient, the WGM snaps back into resonance with the laser in the thermo-optically distorted regime (step **4**). In the self-pulsating regime, the output optical power cycles through the hysteresis curve. (b) 2D axi-symmetric FEM simulation of the thermal strain in a SiN disk resonator structure. The surface color code shows the magnitude of the radial displacement. The deformed shape displays strongly exaggerated displacement amplitude.

Complementary simulations allow verifying that the magnitude of the blue optical shift is independent of residual stress in SiO_2 and SiN layers. Thus the type of instability reported in this article shouldn't be limited to the high-tensile stress SiN employed for our resonators. This is checked experimentally by observing similar instabilities after releasing the stress in a larger fraction of the SiN disks by deeper under-etching. Note that the magnitude of the thermal stress-induced radial displacement of the disks is very small. In the data of Fig. 4, the maximum value of the stress-induced blue shift is 14 pm. In order to account for this shift, the disk's radial displacement needs only be ~1Å, i.e. roughly the diameter of a silicon atom.

For the sake of completeness, the effect of other mechanisms influencing the dynamical behavior of the disk resonators on a slow timescale is discussed in the following. First, a possible influence of the suspended SiN coupling waveguides is ruled out by observing optical instabilities on identically processed standalone SiN disks coupled to a tapered silica fiber [32]. Second, a slow thermal expansion of the sample substrate leading to an optical misalignment at the waveguide injection facet can also safely be ignored: a 1 Kelvin temperature rise produces a displacement of the order of 1 nm.

5. Conclusion

We present chaotic and self-pulsating optical instabilities observed in SiN disk resonators. Their characteristic time spans six orders of magnitude, from hundreds of microseconds to hundreds of seconds. This phenomenon is explained by the interplay between a fast thermo-optic nonlinearity and a much slower thermo-mechanic nonlinearity. A model showing good agreement with experimental data is presented which allows proposing and supporting a credible explanation for the origin of the slow thermal nonlinearity. In this work we show that SiN resonators, despite the absence of two photon absorption, can nonetheless exhibit optical instabilities on a much longer timescale than reported in other systems. We point towards volume optical losses to be responsible for the resonator's thermal instabilities. If a reduction of optical absorption - through better control of the material and surface passivation – is an evident option to control the reported optical instabilities, a proper engineering of the resonator structures can also serve the same goal [33,34]. In our present case, modified designs for the pedestals may lead to reduced instabilities. These aspects become critical for miniature resonators operating at high optical powers.

6. Appendix: optical loss measurements in straight SiN waveguides

In this appendix, we study optical losses in SiN structures in order to support elements of the above analysis and to envision future generation of improved resonators. To this end, we fabricate several versions of straight SiN waveguides using the starting wafers described in section 2. Both fabrication and post-fabrication protocols are varied to study their impact on optical losses. An example of a straight SiN waveguide is shown in Fig. 6(a). Optical loss measurements are performed using a top-view scattering technique [35], where the light intensity scattered by the waveguide is imaged on a CCD camera positioned directly above the guide (Fig. 6(b)). This intensity image is analyzed as an exponential decay of the optical intensity along the guide propagation axis (Fig. 6(c)), and related to a linear loss coefficient α. This technique allows very straightforward monitoring of significant loss levels change, like obtained upon sample annealing (Fig. 6(d)). The top-view scattering technique can be complemented by the Fabry-Pérot interference method [36], when the upwards scattered intensity becomes too weak for a CCD measurement (Fig. 7).

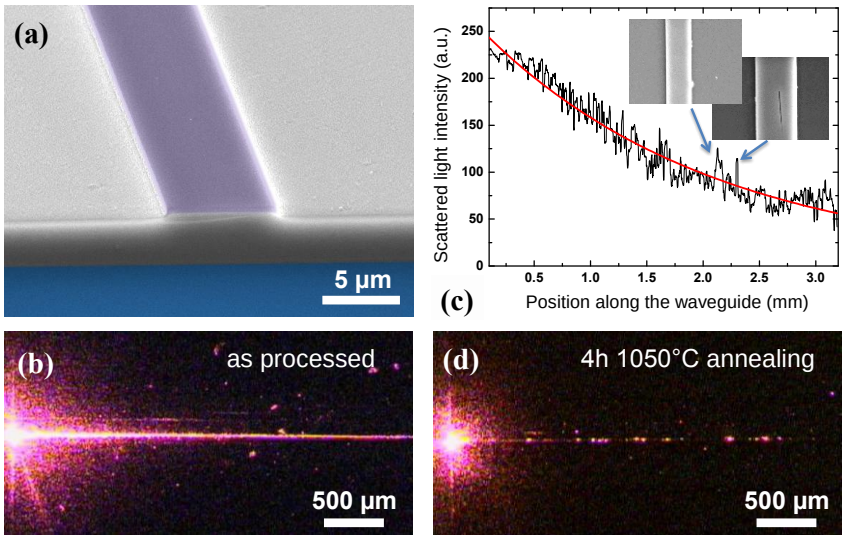

Fig. 6. (a) False color SEM micrograph of a straight SiN waveguide. (b) CCD image top view of an entire SiN waveguide fabricated using protocol 1, with 633 nm wavelength laser light injected at the left sample facet (bright spot at center left) and travelling along the waveguide (bright horizontal line with decaying intensity). (c) Corresponding upwards scattered light intensity as a function of the position along the waveguide, with an exponential decay fit (solid red line). The insets show SEM pictures featuring typical waveguide defects leading to locally increased scattering. The left inset shows an inhomogeneous waveguide width resulting from lithography errors. The right inset shows a crack in the SiN resulting from the high tensile stress. This waveguide was processed using protocol 1. (d) Same waveguide measured after 4h of annealing at 1050°C under N_2 atmosphere. The scattering is essentially caused by isolated defects like the ones shown in the inset of (c), but the output power is now higher than in (b).

Protocol 1

Samples are prepared using standard photolithography and AZ 5214E image-reversal photo resist to define an aluminum metal etch mask. The sample is then etched in a standard PP-RIE machine using CF4 chemistry. The metal etch mask is removed using a hot (80°C) potassium hydroxide (KOH) solution. Waveguides are 3.5 mm long and 2 to 10 µm wide. Waveguides 2 to 5 µm wide are consistently showing higher optical losses, which we interpret as a higher sensitivity to the residual sidewall roughness produced by the photolithography. Waveguides that are 6 to 10 µm wide all exhibit comparable loss levels, showing that sidewall roughness losses are no longer the dominant loss mechanism. For these latter guides, material and top surface losses should now be dominant. We therefore expect the measured linear losses to provide a lower bound for losses in WGM resonators fabricated in a similar fashion. The average loss level measured on 10 such wide waveguides is measured by the scattering method at wavelengths comprised between 543 and 1350 nm. The results are displayed in Table 2. Due to the relatively short length of the guides and the large amount of scattering at the injection and collection end facets, the error bar on these measurements is of the order of ±10%. The measured linear loss coefficients are quite high. The losses measured at 1350 nm would for instance correspond to optical Qs below $2 \cdot 10^4$ on a 10 µm radius SiN disk resonator, where we use the following equation to relate the optical Q and with the loss coefficient α, the free-space wavelength λ_0 and the effective index of the WGM n_{eff}.

$$Q = 2\pi \frac{1}{1 - e^{-\alpha \lambda_0 / n_{eff}}} \qquad (5)$$

Protocol 2

The second protocol is identical to the first, except the aluminum etch mask is removed using a piranha solution (3 H_2SO_4:1 H_2O_2) instead of KOH. Waveguides are 8 µm wide and 2.5 cm long. Using the top-view scattering method, losses at a wavelength of 633 nm are measured with an average value of 0.2 cm^{-1} and the smallest observed values at 0.05 ± 0.01 cm^{-1}. In the infrared, average losses were measured by the Fabry-Pérot interference method and range from 0.15 cm^{-1} at 1490 nm to 0.6 cm^{-1} at 1530 nm. In the 1490 to 1610 nm spectral window, the measured loss level as a function of wavelength shows a maximum at 1530 nm. This is in agreement with [37] which describes a similar feature as absorption induced by Si-H bonds within the material. Our measured loss values translate into optical Qs of $4 \cdot 10^5$ and $1 \cdot 10^5$ respectively, which are in good agreement with the optical Qs of disk resonators presented in this work. The use of the piranha etchant instead of KOH solution to remove the metal mask seems to consistently produce lower optical loss levels. The piranha probably improves the final surface state of the sample.

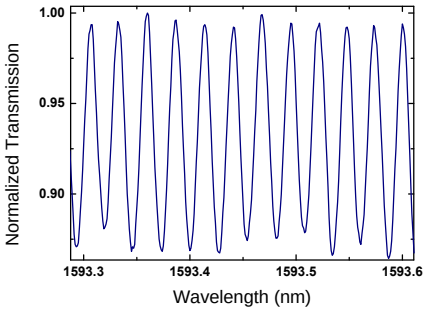

Fig. 7. Transmission spectrum of a 8 µm wide and 2.5 cm long straight waveguide fabricated using protocol 2. Due to the reflectivity of the sample facets, the transmission shows Fabry-Perot interference fringes with 26.6 pm periodicity. Linear losses can be extracted knowing the contrast of the fringes, the facet reflectivity and the sample length. The precision of this method is set by the accuracy in the evaluation of the facet reflectivity and sample length. If the waveguide is multimode, some beating in the fringes' amplitude leads to an overestimation of losses [38].

Effect of post-fabrication annealing

High temperature annealing has been shown to significantly reduce optical loss in SiN waveguides in the near infra-red [37]. Here we anneal the samples fabricated using protocol 1 for 4 hours at 1050°C under a nitrogen atmosphere. This leads to an increase of transmission levels by about an order of magnitude at a wavelength of 633 nm. After this procedure, loss measurements by the top-view scattering technique are no longer possible, as the dominant sources of upwards scattering are now localized scattering defects along the waveguide which are outshining the exponential decay (Fig. 6(d)). However, these defects do not determine optical losses in the waveguide, which remain dominated by distributed loss sources. The Fabry-Perot interference technique leads to estimated losses now below 0.3 cm^{-1} at 1550 nm. For this estimation, the reflectivity of the fundamental guided mode at the cleaved sample facet was computed using FDTD simulations, leading an intensity reflectivity of 5.9%. These losses would correspond to a SiN disk resonator optical Q above $2 \cdot 10^5$. We further found that annealing high tensile stress LPCVD SiN at 1050°C for 1h30 reduces the built in tensile stress. This might or might not be desirable depending on the application. On the waveguides fabricated using protocol 2, an annealing of one hour at 800°C did not produce any measurable change in the linear losses.

Conclusion

Table 2 summarizes the loss measurements carried-out on straight SiN waveguides. Loss levels measured on the waveguides of protocol 1 after annealing are comparable to those measured on the waveguides of protocol 2 before annealing. However, the former show a reduced amount of upwards-scattered light compared to the latter (not shown here). This points towards the interpretation that piranha impacts mostly the surface state of the waveguides, while the 1050°C annealing process would impact volume and/or surface losses.

Table 2. Optical losses measured on straight SiN waveguides at different wavelengths

Wavelength (nm)	543	633	1000	1350	1490	1530	1550
Protocol 1 loss α (cm^{-1})	13.4	7.8	2.6	3.5	-	>7	3
Protocol 1 after 1050 °C annealing	-	~0.15	-	-	<0.3	<0.3	<0.3
Protocol 2 loss α (cm^{-1})	-	0.2	-	-	0.15	0.6	0.3

Acknowledgments

This work was supported by the Franco-German PROCOPE (Egide/DAAD) and the Bavarian-French BFHZ-CCUFB exchange programs. Financial support from the German Excellence Initiative via the Nanosystems Initiative Munich (NIM) is gratefully acknowledged.